coatings

MDPI

Article

Synthesis of Perovskite-Structured $SrTiO_3$ via the Pechini Method and Deposition of Thin Film by RF Magnetron Sputtering: Structural and Photovoltaic Characterization

Mariele Noemi da Silva Diaz [1], Andressa dos Santos [1,*], Luciano Cardoso Dias [2], Mauricio Mazur [1], Fernanda Barbieri [1], Karina Midori Endo [1], Lais Conservan Nogueira [3], Valdirlei Fernandes de Freitas [1], José Antonio Eiras [3], Ivair Aparecido dos Santos [4] and Ricardo Yoshimitsu Miyahara [1]

[1] Postgraduate Program in Nanosciences and Biosciences, Midwestern Paraná State University, Guarapuava 85040-167, Brazil; marielenoemi@gmail.com (M.N.d.S.D.); mauricio.mazur12@gmail.com (M.M.); ferbarbieri21@gmail.com (F.B.); 21614254004@unicentro.edu.br (K.M.E.); vfreitas@unicentro.br (V.F.d.F.); rmiyahara@unicentro.br (R.Y.M.)
[2] Department of Physics, Federal University of Parana, Curitiba 81531-980, Brazil; luciano.dias@ufpr.br
[3] Department of Physics, Federal University of São Carlos, São Carlos 13565-905, Brazil; laisnogueira@df.ufscar.br (L.C.N.); eeiras@df.ufscar.br (J.A.E.)
[4] Department of Physics, State University of Maringá, Maringá 87020-900, Brazil; iasantos@dfi.uem.br
* Correspondence: dossantos.andressa@hotmail.com

Highlights

What are the main findings?

- Dense $SrTiO_3$ ceramic targets were successfully fabricated by SPS.
- $SrTiO_3$ thin films were successfully deposited on FTO by RF Magnetron Sputtering.
- FTO/$SrTiO_3$/CdTe/Au devices exhibited a photovoltaic response.
- The $SrTiO_3$ layer influenced the photoelectric behavior of the device.

What are the implications of the main findings?

- SPS enables the fabrication of suitable $SrTiO_3$ sputtering targets.
- $SrTiO_3$ thin films are promising for oxide-based photovoltaic devices.
- $SrTiO_3$/CdTe heterostructures offer potential for photovoltaic applications.
- The approach supports the development of multilayer thin-film devices.

Abstract

Strontium titanate ($SrTiO_3$) is a stable, non-toxic perovskite oxide that has attracted interest for photovoltaic and optoelectronic applications, including third-generation photovoltaic devices. However, the production of ceramic targets with suitable density and microstructure for sputtering deposition remains a technological challenge. This study investigates a processing route for $SrTiO_3$ ceramic targets and their application in thin-film heterostructures. $SrTiO_3$ powders were synthesized by the Pechini method and densified by Spark Plasma Sintering (SPS), followed by deposition by RF Magnetron Sputtering of thin films. Structural and morphological analyses confirmed the formation of predominantly cubic $SrTiO_3$ and the densified microstructure of the ceramic target. The optical band gap of the films, determined using the Tauc method for an indirect transition, was 3.42 eV for the as-deposited film and 3.35 eV after annealing. The resulting FTO/$SrTiO_3$/CdTe/$CdCl_2$/Au heterostructure exhibited a measurable photoelectric response, with localized photovoltage reaching approximately 400 mV, and photovoltaic parameters of Jsc = 4.32 μA/cm^2, Voc = 9.75 mV, and FF = 21.4%. These findings demonstrate the feasibility of the proposed processing route for producing $SrTiO_3$ thin films and their integration into photoactive heterostructures.

Academic Editor: Octavian Buiu

Received: 17 August 2026
Revised: 9 September 2026
Accepted: 15 September 2026
Published: 18 September 2026

Keywords: strontium titanate; ceramic; RF magnetron sputtering

1. Introduction

A significant contemporary scientific and technological challenge is the shift of the global energy mix to renewable sources, which is motivated by the pressing necessity to reduce greenhouse gas emissions that are linked to the extensive use of fossil fuels. Within this context, the development of sustainable energy solutions and low-carbon technologies have been significantly influenced by public policies and market mechanisms, including carbon credits. The Brazilian Development Bank (BNDES) has supported projects with proven CO_2 emission reductions and high potential for environmental innovation, which have contributed to the consolidation of this landscape in Brazil through institutional initiatives (BNDES, 2026).

In this context, advances in materials science and engineering are inextricably linked to advancements in photovoltaic devices and other energy conversion technologies. Specifically, oxides with a perovskite type are important functional materials because of their exceptional structural flexibility. This flexibility enables the modification of electronic, optical, and dielectric properties through interface control, defect engineering, and doping. Such materials are highly promising for applications in optoelectronic devices, such as solar cells, photodetectors, and energy storage devices, due to their versatility [1,2].

The Pechini method is particularly appealing for the formulation of complex oxide materials, such as $SrTiO_3$, due to its ability to achieve precise control over cation stoichiometry and to promote chemical homogeneity at the molecular level, among the available chemical synthesis routes. In this method, metal ions are complexed with citric acid and subsequently incorporated into a polymeric network through the addition of a polyhydroxy alcohol. This process promotes a uniform distribution of the constituent cations during precursor formation and subsequent thermal treatment [3,4]. For $SrTiO_3$, the polymerized complex route has been reported to facilitate the formation of the perovskite phase and the molecular-scale mixing of Sr and Ti at relatively low temperatures [3]. More recent studies have also demonstrated that the Pechini route can provide greater structural homogeneity and lower calcination temperatures compared with citrate-based combustion methods for $SrTiO_3$-based materials [5]. This makes the Pechini method an appropriate method for the production of $SrTiO_3$ powders with controlled composition and structural properties, which are then used for thin-film deposition and ceramic target fabrication.

Strontium titanate ($SrTiO_3$) is a widely studied model perovskite oxide that is distinguished by its highly tunable electronic properties and its exceptional thermal and chemical stability. Strategies that involve the introduction of oxygen vacancies, transition metal doping, and heterostructure engineering have been shown to significantly improve the photoactive response of intrinsic $SrTiO_3$, despite the fact that its absorption is restricted to the ultraviolet region due to its wide band gap (~3.2 eV) [6,7]. Furthermore, its high dielectric constant and low density of structural defects render it particularly pertinent as a functional layer in advanced photovoltaic architectures, where it functions as an active material, buffer, or electron transport layer in heterojunction based devices [8].

The use of $SrTiO_3$ thin films in photovoltaic devices has been identified as a promising approach for the optimization of charge transport and interface engineering, which has a direct impact on the overall performance of the devices [9,10]. $SrTiO_3$ can function as an electron transport layer or buffer layer on conductive substrates, thereby improving band alignment and reducing interfacial recombination [8]. Additionally, its high dielectric constant makes it easier for electron hole pairs to separate, and its ability to change its

electronic properties through structural flaws like oxygen vacancies lets you change its conductivity and photoactive response [11]. $SrTiO_3$ thin film is a critical material in the pursuit of more durable and efficient devices, as these characteristics contribute to the formation of more efficient junctions in photovoltaic heterostructures, resulting in improved charge extraction and greater operational stability [12].

In this work, $SrTiO_3$ was synthesized by the Pechini method and subsequently densified by Spark Plasma Sintering (SPS) to produce a dense ceramic target using a feasible and accessible laboratory-based approach. The target was subsequently used to deposit $SrTiO_3$ thin films through Radio Frequency (RF) Magnetron Sputtering, thereby establishing a seamless pathway from powder synthesis and target fabrication to thin-film deposition and device integration. The objective was to assess the structural, optical, and photovoltaic properties of $SrTiO_3$/CdTe heterostructures produced by incorporating $SrTiO_3$ as a functional perovskite oxide layer and to demonstrate the feasibility of this approach. This study endeavors to establish a practical pathway for the feasible and accessible laboratory fabrication of $SrTiO_3$ ceramic targets and their subsequent application in thin-film optoelectronic and photovoltaic architectures.

2. Materials and Methods

Strontium nitrate ($Sr(NO_3)_2$) and citric acid were acquired from Êxodo Científica (Sumaré, Brazil). The titanium(IV) butoxide ($C_{16}H_{36}O_4Ti$), Ethylene glycol and isopropyl alcohol were used and purchased from Sigma Aldhich (St. Louis, MO, USA), Fmaia (São Paulo, Brazil) and Synth (Diadema, Brazil), respectively. All reagents were of analytical grade and used as received.

The strontium titanate ceramic powder was synthesized using the Pechini method. The molar ratio used was [Sr]:[Ti]:[citric acid]:[ethylene glycol] = 1:1:4:16 to ensure the stoichiometry of the compound and the development of the polymer matrix. Two solutions were prepared: Solution A contained strontium nitrate and citric acid in an aqueous solution; and Solution B contained titanium butoxide, isopropyl alcohol, and citric acid (a complexing agent for the Ti^{4+} ion). Solutions A and B were mixed, followed by the addition of ethylene glycol to form the polymer resin. The mixture was heated to 100 °C for 30 min until a viscous resin was obtained, which was then calcined at 450 °C at a heating rate of 5 °C/min. The resulting powder was ground and subjected to a calcination process in the temperature range between 800 °C and 1100 °C, under a heating ramp of 5 °C/min for 24 h, to ensure the formation of the perovskite phase. Afterward, the sintering process was conducted using an SPS furnace model, Dr. Sinter 1020, which was manufactured by SPS Syntex Inc (Tokyo, Japan). The calcined powder was inserted into a graphite die with a diameter of 40 mm. The SPS chamber was initially evacuated and subsequently refilled with an Argon atmosphere. The sample was subsequently heated at a constant rate of 100 °C/min from 19 °C to 860 °C, with an axial pressure of 25 MPa maintained throughout the process. The dwell time at the maximum temperature was 20 min.

The $SrTiO_3$ and cadmium telluride (CdTe) thin films were deposited from a densified strontium titanate ceramic target and a commercial 99% pure CdTe target, respectively, using the RF Magnetron Sputtering technique, employing a High Vacuum Magnetron Sputtering Deposition System (HVMSDS) manufactured by Zhengzhou CY Scientific Instrument Co. (CYKY, Zhengzhou, Henan, China). FTO substrates that had been previously cleaned were utilized for the depositions. The $SrTiO_3$ film was deposited at a power of 90 W and an argon flow rate of 20 sccm, resulting in a thickness of 60 nm. The $SrTiO_3$ film was annealed at a temperature of 500 °C for 60 min, with a heating rate of 1 °C/min. After that, the CdTe film was deposited to a thickness of 1 μm using an argon flow rate of 40 sccm and a power of 50 W. The CdTe was subjected to a chemical treatment in a methanol:water (9:1)

solution of 0.03 M cadmium chloride ($CdCl_2$) for 30 s, which was followed by drying in an oven at 100 °C for 5 min. Following this stage, the material underwent thermal treatment in a muffle furnace for 25 min at a temperature of 400 °C, with a heating rate of 2 °C/min. The subsequent step involved the deposition of the gold (Au) layer using a mask that contained holes with a diameter of 3 mm.

The structural characterization of the synthesized material was performed using Attenuated Total Reflectance Fourier Transform Infrared Spectroscopy (ATR-FTIR) conducted on an IR Spirit spectrophotometer (Shimadzu®, serial number A224160, Kyoto, Japan), operating in transmission mode, with a scan range from 400 cm^{-1} to 2000 cm^{-1}. X-ray diffraction (XRD) was conducted using a Shimadzu XRD-7000 diffractometer (Kyoto, Japan), which was equipped with a Cu tube (λ = 1.5406 Å). The instrument operated at 40 kV and 30 mA in the 20° to 80° range, with a step size of 0.02°. Raman spectroscopy was performed on a MicroRaman system, model Senterra (Bruker Optik GmbH, Ettlingen, Germany), using a laser with a wavelength of 532 nm, a power of 2.0 mW, a 20x objective, and 30 acquisitions with an integration time of 1 s per acquisition. The morphological analysis of the powder and densified material was conducted using a Scanning Electron Microscope (SEM) equipped with a Tescan Vega G4 (Brno, Czech Republic), serial number 125-0010, in conjunction with Energy Dispersive Spectroscopy (EDS), and the microstructural analyses of the thin films were performed using an FEI Scios DualBeam FIB/SEM microscope (Waltham, MA, USA), combining field-emission scanning electron microscopy (FE-SEM) with focused ion beam (FIB) technology. The optical behavior of the $SrTiO_3$ thin film was investigated using ultraviolet-visible (UV-vis) spectroscopy on a Shimadzu UV-1900i (Kyoto, Japan) with a wavelength range of 280 nm to 600 nm. This allowed for the determination of the absorption region and the estimation of the optical band gap using the Tauc method.

The J-V characteristics of the devices were evaluated under simulated solar illumination using a xenon lamp equipped with an AM1.5 filter. During the measurements, the devices were continuously illuminated while the voltage was varied and the corresponding current was recorded. The measured current was normalized to the active area of each device to obtain the current density (J), allowing the a photovoltaic response of the $SrTiO_3$/CdTe heterostructure and the reference device to be evaluated and compared. In addition, time-dependent photovoltage measurements and open-circuit voltage (Voc) mapping were performed using the Photoresponse Spot Mapper system (Guarapuava, Brazil) (BR10202402353) in conjunction with an Agilent Technologies 34405A digital multimeter (Agilent Technologies, Inc., Santa Clara, CA, USA). The measurements were conducted under continuous illumination from the xenon lamp equipped with an AM1.5 filter, enabling the monitoring of the potential difference generated by the devices as a function of illumination and measurement position. These measurements were used to evaluate the spatial distribution and temporal stability of the photovoltage generated by the investigated heterostructures.

3. Results and Discussion

3.1. Structural Analysis

Attenuated Total Reflectance Fourier Transform Infrared Spectroscopy was conducted on $SrTiO_3$ ceramic powder samples that were calcined at 450 °C, 900 °C, and 1100 °C, as illustrated in Figure 1. $SrTiO_3$ is confirmed by the presence of intense bands, primarily in the 400–800 cm^{-1} range, which are attributed to the typical vibrations of titanate groups, as described in the literature [3,13]. The perovskite lattice is characterized by the peaks at approximately 481 cm^{-1}, which are associated with Ti-O stretching vibrations, and at 541 cm^{-1}, which are attributed to Sr-Ti-O bonds [14]. The presence of bands at 697 cm^{-1}, which are associated with Sr-O vibrations, and at 705 cm^{-1}, which are again related to

Ti-O bonds, suggests that the structural organization of $SrTiO_3$ has commenced, even at intermediate temperatures [13–15]. In the sample that was calcined at 450 °C, the Pechini method still detects bands associated with organic residues and carbonates. This is demonstrated by signals around 856–858 cm^{-1}, which are attributed to the symmetric stretching of the carbonate ion (CO_3^{2-}), as well as by bands at 1071 cm^{-1}, which are related to C-O vibrations, and at 1445–1450 cm^{-1}, which are also attributed to carbonate groups [13], these bands are relatively broad and poorly defined.

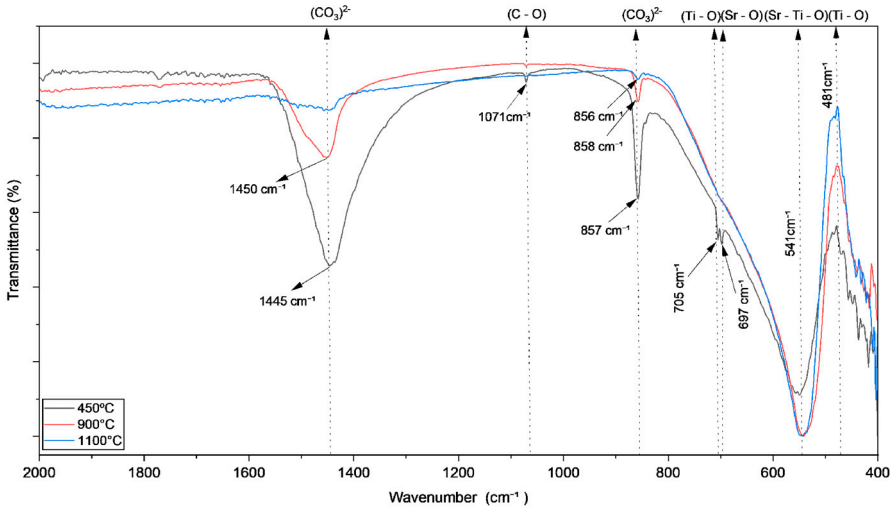

Figure 1. ATR-FTIR Spectra of $SrTiO_3$ calcined samples.

The intensity of these characteristic bands is significantly reduced as the temperature increases to 900 °C, which is accompanied by a more precise definition of the characteristic vibrations of $SrTiO_3$. This outcome suggests that the crystallization process is advancing, which is consistent with the findings of studies that identify the 800–900 °C range as a critical threshold for the structural transition [14,15]. The $SrTiO_3$ perovskite phase is nearly fully formed in the sample treated at 1100 °C, as evidenced by the near complete disappearance of the bands associated with carbonates and the increase in the intensity of the vibrations specific to titanates [15]. This finding is consistent with the findings of Roy and Bera (2005) and other studies that suggest the stabilization of the crystal structure at temperatures exceeding 1000 °C [15]. According to the ATR-FTIR results, the sample that was calcined at 1100 °C exhibited a significant reduction in the bands associated with organic residues and carbonates, as well as a greater definition of the vibrational bands characteristic of the perovskite structure.

Figure 2a shows the XRD diffractograms of the $SrTiO_3$ ceramic powder samples calcined at 450 °C, 900 °C, and 1100 °C. The peaks are in accordance with the ICSD 080874, 9015662, 015195 data, which displays the typical reflections of the cubic perovskite structure of $SrTiO_3$ at 1100 °C, which is a member of the $Pm\bar{3}m$ space group. The lattice parameters calculated from the main reflections are consistent with those reported in the literature, confirming the correct structural formation of $SrTiO_3$. The high intensity and narrow peak broadening in the synthesized material suggest a high degree of crystallinity and the predominance of the perovskite phase [14]. A low-intensity peak was also observed at $2\theta \approx 31.78°$, which was likely the result of the interaction between strontium-rich species and atmospheric CO_2 during or after calcination [6]. This peak was attributed to the residual presence of $SrCO_3$ [3]. However, the low intensity of this reflection suggests that the secondary phase is present in only trace amounts, without compromising the predominant formation of the perovskite structure [9,14]. The material revealed a well-

developed crystalline structure, as evidenced by its high degree of crystallinity and an average crystallite size of 75.3 nm, which ranged from 67.1 to 83.5 nm.

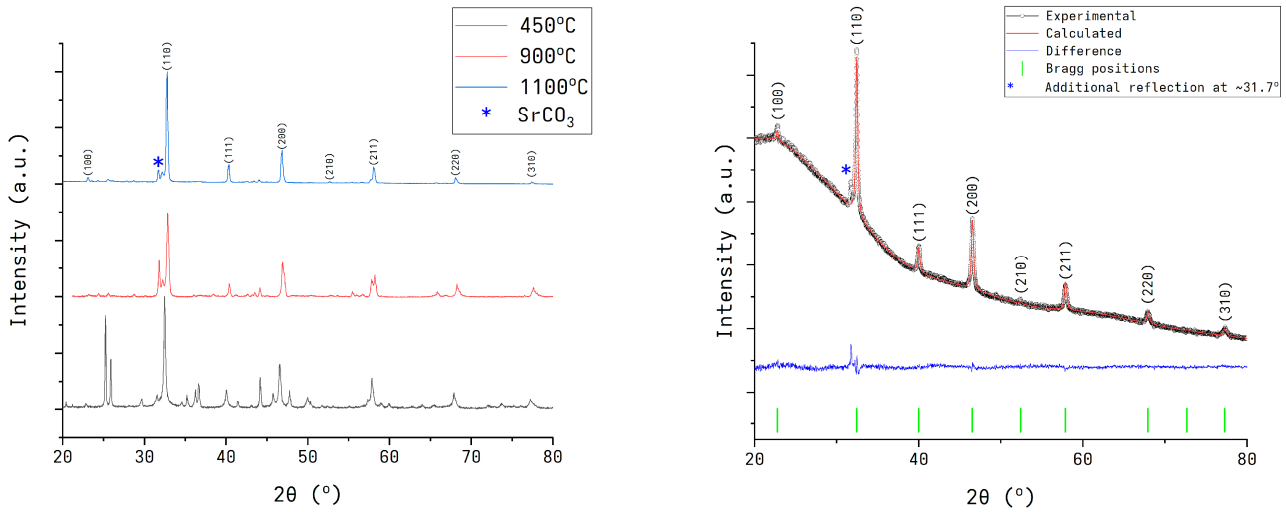

Figure 2. XRD diffractogram of the $SrTiO_3$ samples of the (**a**) ceramic powder calcined and (**b**) thin-film deposited on glass by RF Magnetron Sputtering.

Figure 2b shows the X-ray diffraction pattern and Rietveld refinement of the $SrTiO_3$ thin-film deposited on glass by RF Magnetron Sputtering. The diffraction pattern was satisfactorily described using the cubic $SrTiO_3$ structure with space group $Pm\bar{3}m$, yielding a lattice parameter of a = 3.90032 Å (ICSD 080874, 9015662, 015195). The refinement converged with R_{wp} = 1.75%, R_p = 1.32%, R_{exp} = 1.67, and χ^2 = 1.099, confirming that cubic $SrTiO_3$ is the predominant crystalline phase in the deposited film. A weak additional reflection is observed at approximately 2θ ≈ 31.7–31.8o, which is not reproduced by the cubic $SrTiO_3$ structural model. Although a reflection in this angular region may be associated with residual $SrCO_3$, the absence of other characteristic $SrCO_3$ reflections, particularly those expected at approximately 25.4°, 29.7°, 36.5°, 41.5–41.7°, and 44.4–44.5° [16], does not provide sufficient evidence to support $SrCO_3$ as a significant crystalline secondary phase. Therefore, this weak reflection cannot be unambiguously assigned to $SrCO_3$, and further structural evidence would be required for definitive phase identification.

The Raman spectrum of $SrTiO_3$ exhibits bands that are associated with vibrational modes that are activated by second-order effects and local symmetry breaking in the crystal lattice (Figure 3). Although the cubic perovskite structure, $Pm\bar{3}m$, is Raman inactive in the first-order at room temperature, the presence of polycrystallinity, structural defects, and residual stresses induces the relaxation of selection rules, rendering these modes visible [17]. This phenomenon is extensively documented in the literature for synthetic and polycrystalline $SrTiO_3$ [3,11,18].

The "soft mode" of the structure is identified as a band at approximately 105 cm^{-1} in the low-frequency region, which is attributed to the TO_1 mode [19]. This mode is associated with the vibrations of the Sr^{2+} ion in relation to the TiO_6 octahedron [11]. The bands at approximately 150, 186, and 206 cm^{-1} are linked to modes that involve Sr^{2+} displacements and TiO_6 octahedron vibrations, while the band at approximately 287 cm^{-1} is the result of O-Ti-O bending vibrations, which are indicative of local distortions in the lattice [20]. In conjunction, these signatures suggest the existence of surface effects and structural distortions in the material [21].

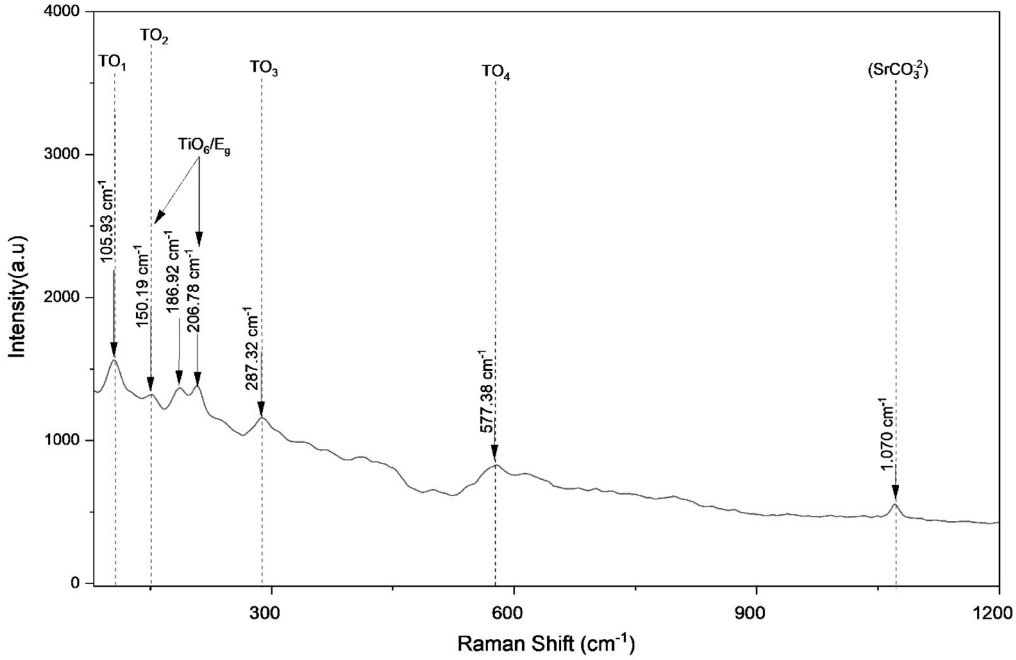

Figure 3. The Raman spectra of $SrTiO_3$ calcined powder at 1100 °C.

Furthermore, the band at 577 cm^{-1} is linked cm^{-1} the TO_4 mode, which is indicative of the transverse stretching of the Ti-O bonds in the TiO_6 octahedron [22]. Its activation implies the presence of structural defects and a local break in inversion symmetry. A narrow band is also observed at approximately 1070 cm^{-1}, which is attributed to the ν_1 mode of the carbonate group, a characteristic of $SrCO_3$ [22–24]. This band provides evidence of a secondary phase that was detected by the high surface sensitivity of the Raman technique.

Figure 4 shows the evolution of the linear shrinkage of the $SrTiO_3$ sample, in millimeters, along with the temperature variation during the sintering process. At the outset of the cycle, the gradual application of uniaxial pressure is observed with rapid shrinkage, which is the consequence of the initial compaction of the powder. The displacement remains nearly constant until the pressure reaches 25 MPa, which is approximately 530 °C. Above this temperature, progressive shrinkage begins, which intensifies as the temperature rises.

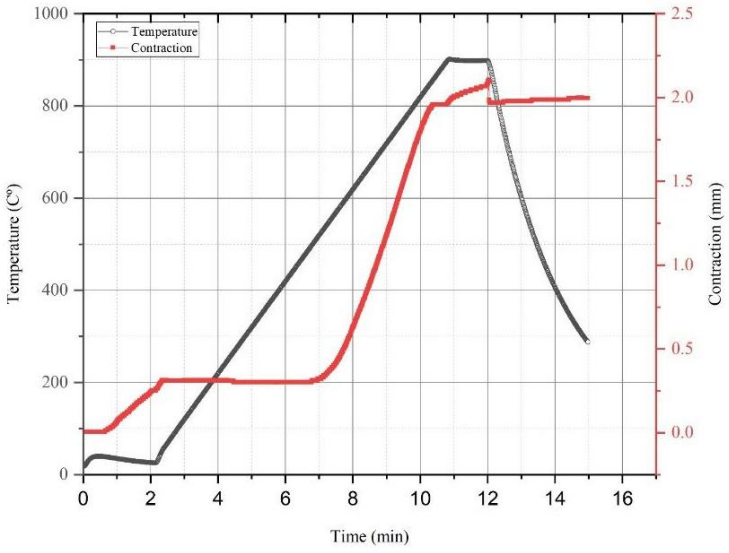

Figure 4. Effect of the SPS temperature on the displacement rate over time during the sintering process.

The densification process is most intense in the temperature range of 740 °C, as evidenced by the analysis of the variation in displacement as a function of time. Shrinkage continues as the temperature rises, reaching a cumulative displacement of approximately 8.56 mm at the end of the plateau. The displacement stabilizes at the conclusion of this period, suggesting that no additional substantial deviations in shrinkage occurred during the final phase of the cycle.

The morphological evolution of $SrTiO_3$ from the calcined powder to the ceramic target and the thin-films before and after annealing treatment can be evaluated using the SEM micrographs exhibited in Figure 5a–d. In Figure 5a, $SrTiO_3$ calcined at 1100 °C demonstrates particles with irregular contours, a broad size distribution, and a strong tendency toward agglomeration. These characteristics are frequently associated with ceramic powders obtained through chemical routes, particularly the Pechini method, following heat treatments at high temperatures. The particles' approach and coalescence are facilitated by their high surface energy, which leads to the formation of agglomerates and a decreased degree of particle individuality [25].

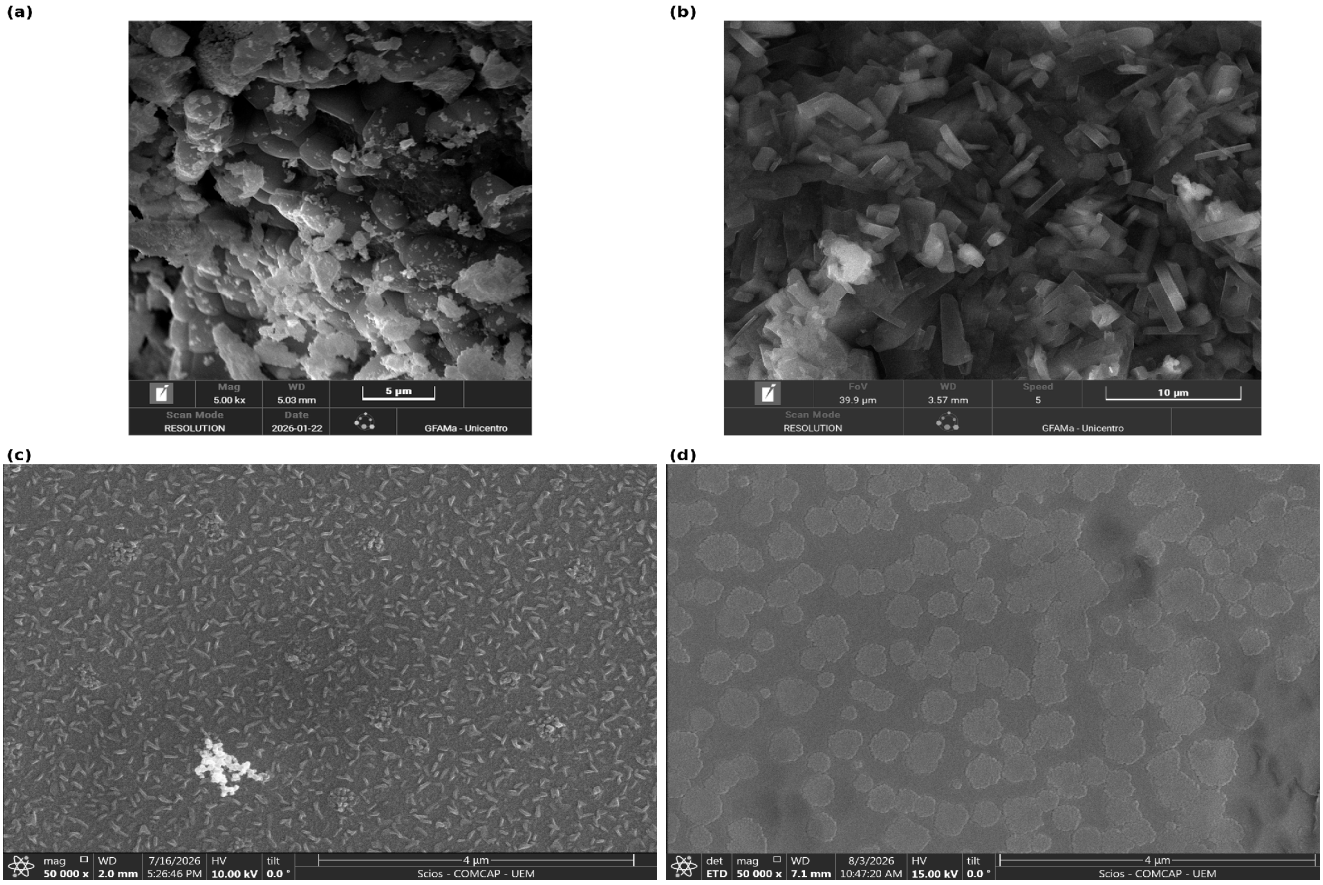

Figure 5. SEM micrographs of $SrTiO_3$: (**a**) calcined powder at 1100 °C; (**b**) SPS ceramic target; (**c**) as-deposited thin film; and (**d**) after annealing thin film.

The Pechini method contributed to the homogenization of Sr^{2+} and Ti^{4+} cations during the synthesis of $SrTiO_3$. Citric acid functions as a complexing agent in this process, forming complexes with the metal cations. Ethylene glycol facilitates polyesterification and the formation of a polymeric matrix, which maintains the cations' molecular distribution and minimizes their segregation during heat treatment. Kakihana et al., (1998) demonstrated that the polymerized complex route is preferable for the formation of the perovskite phase in the $SrTiO_3$ system [3]. This is due to the high homogeneity of the Sr-Ti-citrate precursor,

which enables the production of $SrTiO_3$ at relatively low temperatures. Subsequent studies also indicate that the Pechini route can result in greater structural homogeneity when compared to other citrate-based routes [3,5] Thus, the choice of method was primarily related to controlling the chemical homogeneity of the precursors and their ability to promote the formation of the $SrTiO_3$ phase.

In Figure 5b, the micrograph of the $SrTiO_3$ ceramic target produced by Spark Plasma Sintering illustrates a densified microstructure with a heterogeneous grain size distribution and low apparent porosity. The non-equilibrium conditions of SPS may have promoted anisotropic grain growth, as indicated by elongated or acicular regions interspersed with fine, well-compacted grains [14,25]. This morphology is consistent with the accelerated diffusion and localized recrystallization facilitated by the combined action of pulsed electric current and uniaxial pressure [26]. The observed microstructural evolution demonstrates the efficiency of SPS in promoting densification, pore elimination, and grain-growth control within a short processing time [27]. This behavior is in accordance with reports that SPS can produce dense and homogeneous microstructures at temperatures substantially lower than those of conventional sintering [24,27,28].

Figure 5c illustrates that the $SrTiO_3$ film's surface in its as-deposited state exhibits a diverse morphology, including fine particles that adhere to one another, grains that are round or partially faceted, elongated structures, and agglomerates that are grouped together in specific regions. It is evident that the substrate is covered in a uniform surface layer on a micrometer scale, despite the heterogeneity. Local conditions of nucleation, growth, and coalescence during RF Magnetron Sputtering deposition, as well as the FTO surface's influence, may be associated with the occurrence of various morphologies [29–31]. After heat treatment (Figure 5d), the $SrTiO_3$ film exhibits a more homogeneous morphology, with a relatively uniform distribution of predominantly rounded grains. This evolution may be associated with thermally activated surface diffusion and rearrangement of deposited species, promoting grain coalescence during annealing [30].

EDS analysis (Figure 6) confirmed the exclusive presence of the elements Sr, Ti, and O, indicating that the perovskite phase was preserved following SPS. An increase in Ti content and a trend toward the ideal composition were observed in the stoichiometric ratio in comparison to the precursor powder [32]. The intensification of cationic diffusion mechanisms during sintering and the decomposition of strontium-rich secondary phases may be contributing factors to this change [28]. The results suggest that SPS not only enhances the densification of $SrTiO_3$ but also fosters a greater degree of chemical homogenization and structural stabilization.

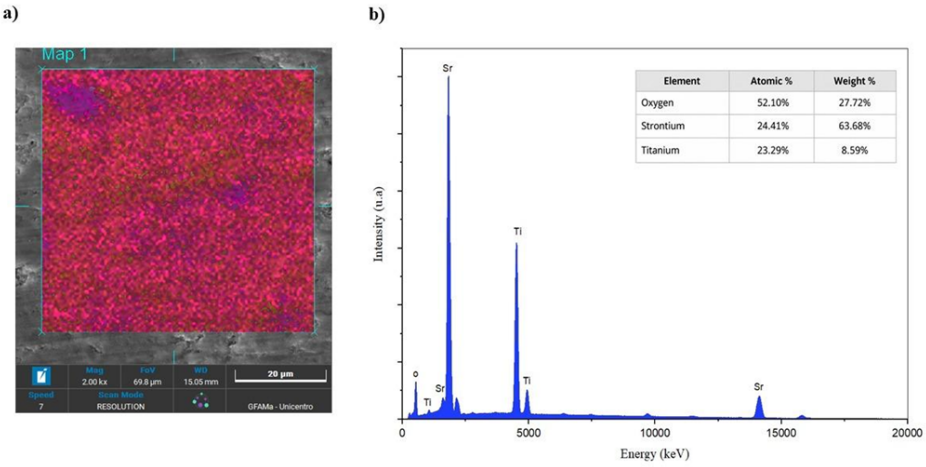

Figure 6. Dark field image (**a**) and EDS mappings (**b**) of Ti and Sr at a grain boundary in $SrTiO_3$ densified.

3.2. Optical Properties

Figure 7 illustrates that UV−Vis spectroscopy was implemented to assess the optical absorption characteristics of the $SrTiO_3$ thin film as-deposited and annealed. The film exhibits a pronounced absorption edge in the ultraviolet region, indicating that its optical absorption is predominantly located in this spectral range. The absorption profile illustrates the optical response of the deposited $SrTiO_3$ film and its potential for use in photovoltaic and optoelectronic devices. The band gap energy of the thin film of the $SrTiO_3$ densified target was estimated using the Tauc plot method, considering an indirect optical transition, as shown in the inset plots of Figure 7. Two absorption regions were identified, with a band gap value of 3.42 eV and an absorption onset at approximately 340 nm (Figure 7a) and 3.35 eV with an absorption onset at approximately 360 nm (Figure 7b). These values are consistent with the range commonly reported for $SrTiO_3$, which typically varies from 3.2 to 3.4 eV [6].

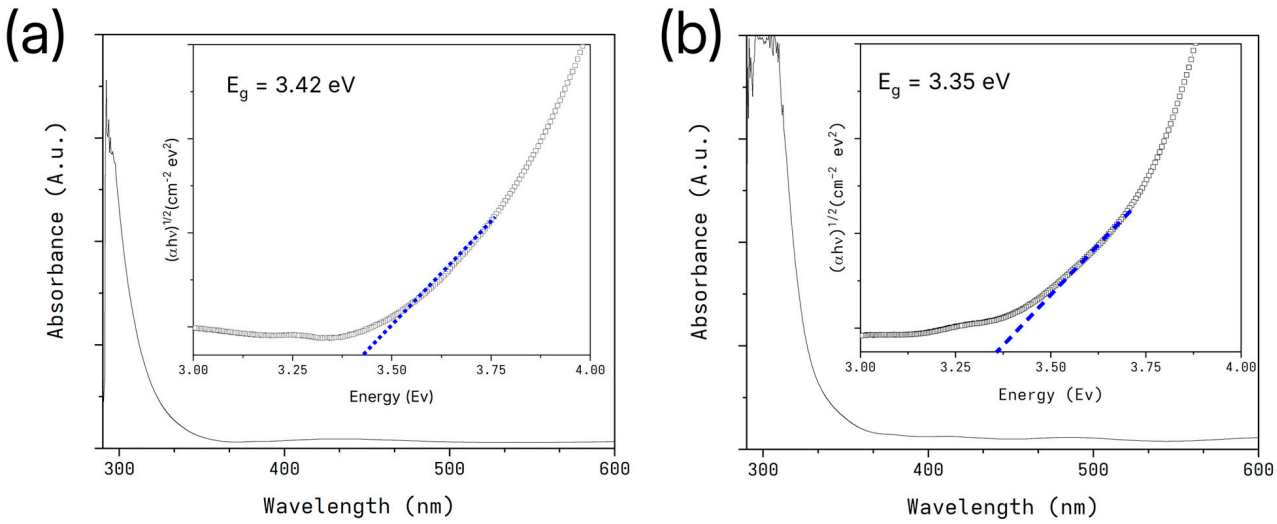

Figure 7. The UV-Visible spectra with inset Tauc plots of the $SrTiO_3$ thin film (**a**) as-deposited thin film and (**b**) after annealing thin film. The extrapolation of the fitted line (blue dash line).

The difference in the optical band gap observed between the as-deposited and annealed films can be associated with the thermal treatment, which promotes structural and microstructural reorganization of the deposited layer. In RF-sputtered $SrTiO_3$ films, post-deposition annealing has been reported to promote crystallization, increase grain size, and modify the optical properties and band gap of the films [33,34]. In this context, the observed shift in the absorption edge can be related to the reorganization of the film during annealing, including changes in crystallinity, structural disorder, and defect states, which consequently affect the electronic transitions [33,34]. Overall, the obtained values indicate that the $SrTiO_3$ thin film exhibits strong ultraviolet absorption and an optical band gap characteristic of the perovskite oxide.

3.3. Photoresponse and Photoelectric Properties

The photo response mapping technique was employed to investigate the spatial distribution of the spatial distribution of the open-circuit voltage (V_{oc}) across the device the composite cell, which consists of FTO/$SrTiO_3$/CdTe/$CdCl_2$/Au thin films (Figure 8). The illuminated regions of the film exhibit a significant increase in V_{oc}, which suggests the establishment of a photoinduced potential difference and the system's potential to convert light energy into electrical energy [31]. Points that contained the gold (Au) metal layer exhibited the highest potential values, which reached approximately 400 mV when

illuminated. It is evident from this behavior that the $SrTiO_3$/CdTe interface is essential for the separation and collection of photogenerated charge carriers, thereby improving the device's V_{oc}.

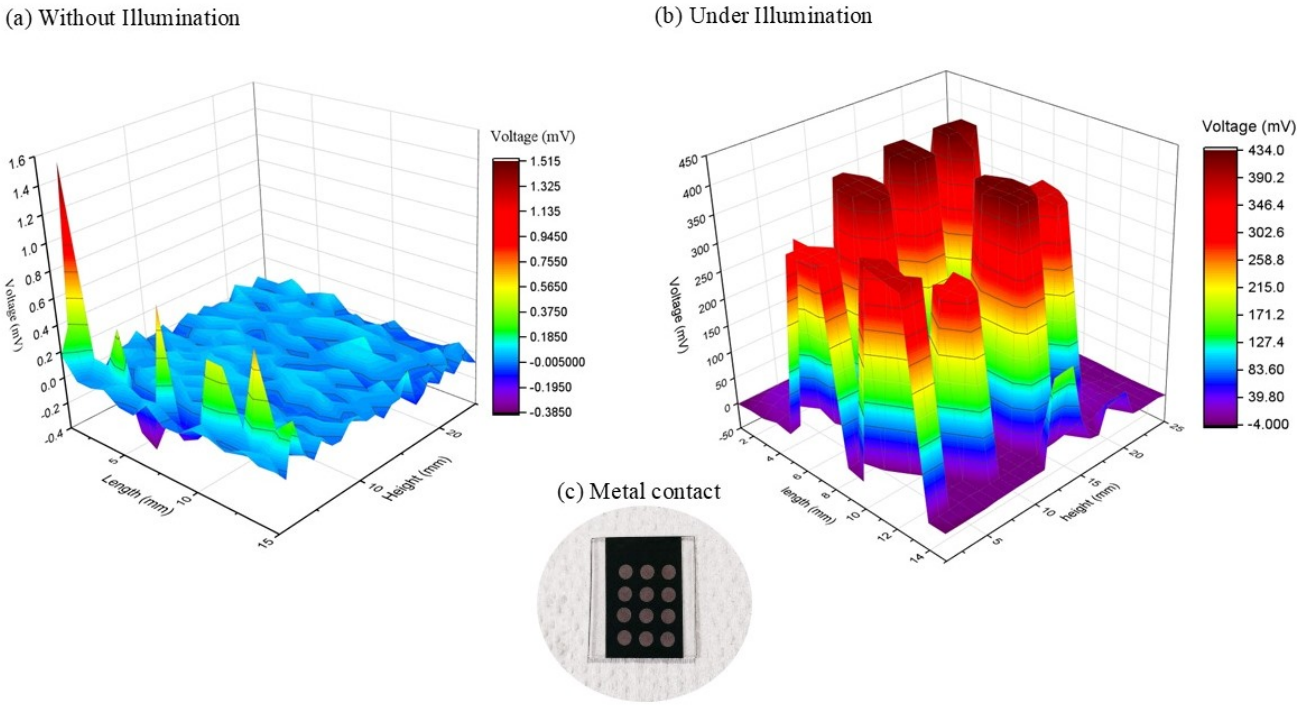

Figure 8. Spatial V_{oc} mapping of the FTO/$SrTiO_3$/CdTe/$CdCl_2$/Au cell sample (**a**) in the dark, (**b**) under illumination and (**c**) device with a metal contact.

Moreover, the spatial V_{oc} mapping revealed that the photovoltage levels of the various Au contacts were relatively similar, suggesting a predominantly homogeneous photoelectric response throughout the active regions of the thin film. The overall spatial uniformity was not compromised by the small local variations that were observed. These differences may be attributed to minor heterogeneities that are inherent to the deposition process, such as variations in film thickness, surface roughness, microstructural features, or local differences in the quality of the interfaces between the layers [30,35].

In general, the V_{oc} mapping supports the electrical analyses that were previously presented, confirming the generation of photovoltage under light irradiation and illustrating that the photoelectric response is concentrated within the active regions defined by the Au electrodes. The uniform charge generation and collection across the investigated regions is further supported by the homogeneous spatial distribution of the response, which supports the proper functioning of the multilayer heterostructure developed in this work.

Under light irradiation, the photoelectric behavior of the FTO/$SrTiO_3$/CdTe/$CdCl_2$/Au device is illustrated by the voltage-versus-time curve in Figure 9. The photovoltage experiences a rapid increase upon illumination, culminating in a maximum value of approximately 47 mV/cm^2. This abrupt increase supports the efficient generation and separation of photoinduced charge carriers in the system, a characteristic of photoactive semiconductor materials employed in photovoltaic and photoelectrochemical devices [2,36].

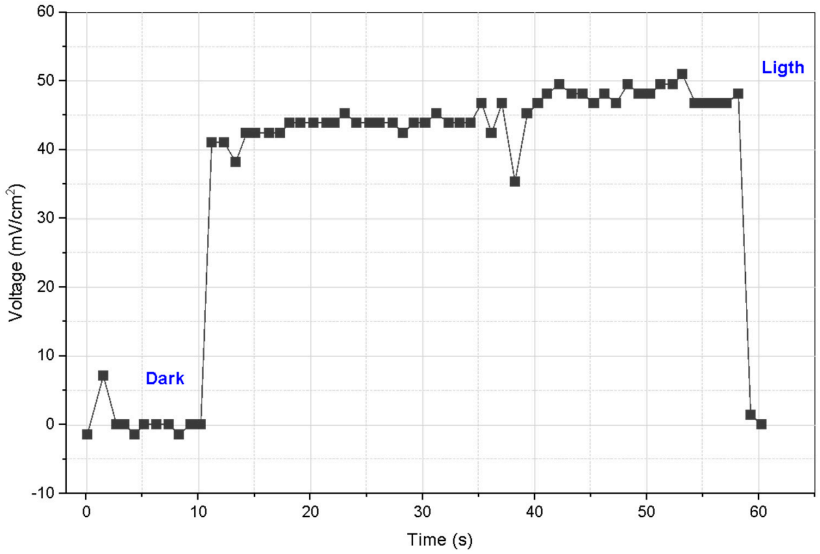

Figure 9. Voltage versus time curve for the FTO/$SrTiO_3$/CdTe/$CdCl_2$/Au cell under illumination.

3.4. Photovoltaic Properties

Under light irradiation, a photovoltaic response of the FTO/$SrTiO_3$/CdTe/$CdCl_2$/Au device was evaluated through the current density-voltage (J-V) characteristic shown in Figure 10. The device exhibited a short-circuit current density (J_{sc}) of approximately 4.32 μA/cm^2 and an open-circuit voltage (V_{oc}) of 9.75 mV. The simultaneous occurrence of a non-zero current density at zero applied voltage and a finite open-circuit voltage indicates the generation and separation of photogenerated charge carriers within the heterostructure, a characteristic behavior of photoactive semiconductor materials employed in photovoltaic and photoelectrochemical devices [2,36]. The current density progressively decreases as the applied voltage approaches V_{oc}, reaching approximately zero at 9.75 mV. A fill factor (FF) of 21.4% was obtained, corresponding to a maximum electrical power density of approximately 9.0 nW/cm^2.

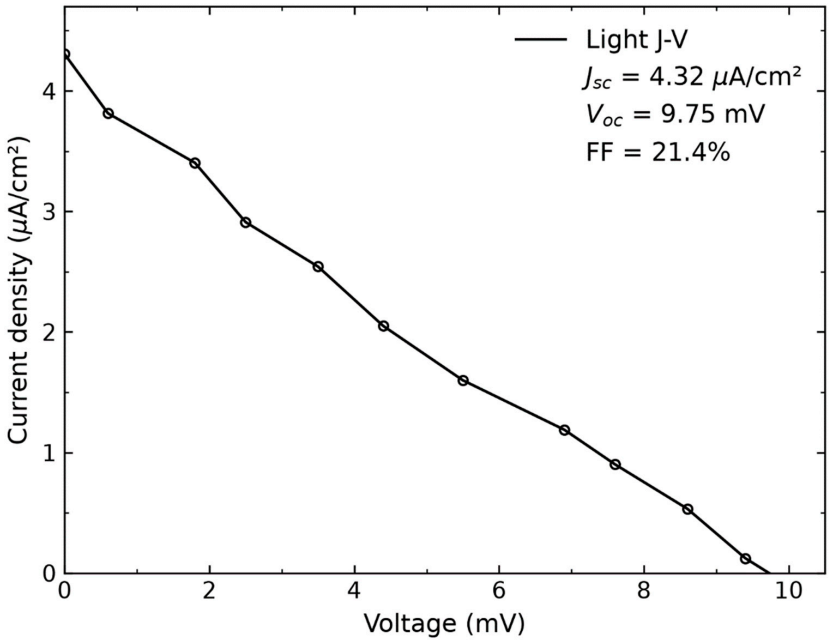

Figure 10. Current density-voltage (J-V) characteristic of the FTO/$SrTiO_3$/CdTe/$CdCl_2$/Au device under illumination. The extracted photovoltaic parameters were J_{sc} = 4.32 μA/cm^2, V_{oc} = 9.75 mV, and FF = 21.4%.

The observed J-V behavior may also be influenced by the microstructural characteristics of the thin-film achieved through sputtering, including surface heterogeneities, grain size, and interfaces between the $SrTiO_3$/CdTe layers. These factors directly affect the transport and mobility of charge carriers [8]. However, the measurable J_{sc} and V_{oc} demonstrate that the heterostructure is photoactive and capable of generating electrical power under illumination.

4. Conclusions

$SrTiO_3$ powders were potential synthesized by the Pechini method, with the sample calcined at 1100 °C showing well-defined titanate bands and reduced carbonate species. XRD and Raman analyses confirmed the predominant cubic perovskite structure, with an average crystallite size of 75.3 nm. The SPS ceramic target exhibited a highly densified microstructure with low apparent porosity, while EDS confirmed the presence of Sr, Ti, and O.

$SrTiO_3$ thin films deposited by RF Magnetron Sputtering were characterized by XRD and SEM, confirming the predominant cubic structure and morphological evolution after annealing. The indirect optical band gap was 3.42 eV for the as-deposited thin film and 3.35 eV after annealing. The FTO/$SrTiO_3$/CdTe/$CdCl_2$/Au heterostructure exhibited photoelectric and a photovoltaic responses, with a photovoltage of approximately 400 mV in localized regions and J_{sc} = 4.32 μA/cm^2, V_{oc} = 9.75 mV, and FF = 21.4%. These results demonstrate the photoactive behavior of the developed heterostructure and the potential of RF-sputtered $SrTiO_3$ thin films for photovoltaic and optoelectronic applications.

Author Contributions: Conceptualization, M.N.d.S.D., A.d.S., V.F.d.F. and R.Y.M.; methodology, M.N.d.S.D., A.d.S., L.C.N., V.F.d.F. and R.Y.M.; formal analysis, M.N.d.S.D., A.d.S., L.C.D., M.M., F.B., L.C.N., V.F.d.F. and I.A.d.S.; investigation, M.N.d.S.D., A.d.S., M.M., K.M.E., L.C.N., V.F.d.F., J.A.E. and R.Y.M.; resources, M.N.d.S.D., A.d.S., M.M., L.C.N. and V.F.d.F.; data curation, M.N.d.S.D., A.d.S., M.M., K.M.E., L.C.N., J.A.E. and I.A.d.S.; writing—original draft preparation, M.N.d.S.D., A.d.S. and M.M.; writing—review and editing, V.F.d.F. and R.Y.M.; visualization, J.A.E. and I.A.d.S.; supervision, V.F.d.F., J.A.E., I.A.d.S. and R.Y.M. All authors have read and agreed to the published version of the manuscript.

Funding: This research was funded by the National Council for Scientific and Technological Development (INCT/CNPq), Brazil, through a Postdoctoral Junior Fellowship (PDJ), Grant No. 406322/2022-8; and the National Fund for Scientific and Technological Development (FNDCT), through the CT-Energ, Grant No. 406099/2022-7.

Institutional Review Board Statement: Not applicable.

Informed Consent Statement: Not applicable.

Data Availability Statement: The data used to support the findings of this study are available from the corresponding author upon request.

Acknowledgments: The authors gratefully acknowledge the institutional and technical support provided by the Araucária Foundation (PI 05/2023 – FA), the MatFerrce group, the New Zero-Carbon Energy Research and Innovation Arrangement, the Applied Materials Physics Group (GFAMa) from Midwestern Paraná State University, and the Secretariat of Science, Technology and Higher Education of Paraná (SETI), through the Paraná Fund (Fundo Paraná). The authors also sincerely thank Julia de Oliveira Primo, from ChIPS, Research Institute for Materials Science and Engineering, Belgium, for performing the Raman spectroscopy measurements and for her valuable contribution to the characterization of the samples.

Conflicts of Interest: The authors declare no conflicts of interest.

Abbreviations

The following abbreviations are used in this manuscript:

BNDES	Brazilian Development Bank
SPS	Spark Plasma Sintering
RF	Radio Frequency
HVMSDS	High Vacuum Magnetron Sputtering Deposition System
FTO	Fluorine-doped tin oxide Substrate
sccm	Standard Cubic Centimeters per Minute
ATR-FTIR	Attenuated Total Reflectance Fourier Transform Infrared Spectroscopy
XRD	X-ray diffraction
SEM	Scanning Electron Microscope
FE-SEM	Field-Emission Scanning Electron Microscopy
FIB	Focused Ion Beam
EDS	Energy Dispersive Spectroscopy
UV-vis	Ultraviolet-visible spectroscopy
Rwp	Weighted Profile Residual
Rp	Profile Residual
Rexp	Expected R-factor
Voc	Open-circuit voltage

References

1. Rondinelli, J.M.; Spaldin, N.A. Structure and Properties of Functional Oxide Thin Films: Insights From Electronic-Structure Calculations. *Adv. Mater.* **2011**, *23*, 3363–3381. [CrossRef]
2. Grätzel, M. Photoelectrochemical cells. *Nature* **2001**, *414*, 338–344. [CrossRef]
3. Kakihana, M.; Okubo, T.; Arima, M.; Nakamura, Y.; Yashima, M.; Yoshimura, M. Polymerized Complex Route to the Synthesis of Pure $SrTiO_3$ at Reduced Temperatures: Implication for Formation of Sr-Ti Heterometallic Citric Acid Complex. *J. Sol-Gel Sci. Technol.* **1998**, *12*, 95–109. [CrossRef]
4. de Souza, M.; Candeia, R.; Souza, S.; Chaves, A.; Lima, S.; Longo, E.; Soledade, L.; Santos, I.; Souza, A. Synthesis and characterization of Sr1−xMgxTiO$_3$ obtained by the polymeric precursor method. *Mater. Lett.* **2005**, *59*, 549–553. [CrossRef]
5. Mizera, A.; Drożdż, E. Properties of cobalt-doped $SrTiO_3$ derived from two methods: The modified Pechini method and the citrate combustion method. *J. Therm. Anal. Calorim.* **2023**, *148*, 9947–9962. [CrossRef]
6. van Benthem, K.; Elsässer, C.; French, R.H. Bulk electronic structure of $SrTiO_3$: Experiment and theory. *J. Appl. Phys.* **2001**, *90*, 6156–6164. [CrossRef]
7. Chambers, S.A. Epitaxial Growth and Properties of Doped Transition Metal and Complex Oxide Films. *Adv. Mater.* **2009**, *22*, 219–248. [CrossRef] [PubMed]
8. Kozuka, Y.; Kim, M.; Ohta, H.; Hikita, Y.; Bell, C.; Hwang, H.Y. Enhancing the electron mobility via delta-doping in $SrTiO_3$. *Appl. Phys. Lett.* **2010**, *97*, 222115. [CrossRef]
9. Rogé, V.; Garlisi, C.; Popa, P.L.; Menguelti, K.; Michel, M.; Vergne, C.; Wagner, E.; Maudez, W.; Benvenuti, G.; Pistillo, B.R.; et al. $SrTiO_3$ thin film photoanodes fabricated by combinatorial chemical beam vapour deposition: Intricate connection between elemental composition and thin films' properties. *J. Mater. Chem. A* **2024**, *12*, 15227–15239. [CrossRef]
10. Jiang, J.; Zhou, Y.; Zhang, J.-L.; Gao, K.; Pan, J.; Dong, P. Accelerating the charge separation from the Schottky junction effect of Pd-loaded Al: $SrTiO_3$ for highly efficient photocatalytic hydrogen evolution. *Int. J. Hydrogen Energy* **2024**, *82*, 646–654. [CrossRef]
11. Chapron, D.; Cordero, F.; Fontana, M.D. Characterization of oxygen vacancies in $SrTiO_3$ by means of anelastic and Raman spectroscopy. *J. Appl. Phys.* **2019**, *126*, 154101. [CrossRef]
12. Sze, S.; Ng, K.K. Physics and Properties of Semiconductors—A Review. *Phys. Semicond. Devices* **2006**, *3*, 5–75. [CrossRef]
13. Hikmah, D.N.; Sandi, D.K.; Nurosyid, F.; Iriani, Y. Effects of Sintering Temperature and Holding Times on the Microstructure and Chemical Bond of Strontium Titanate ($SrTiO_3$). *J. Phys. Conf. Ser.* **2021**, *2110*, 012011. [CrossRef]
14. Rocha-Rangel, E.; Pech-Rodríguez, W.J.; López-Hernández, J.; Calles-Arriaga, C.A.; Armendáriz-Mireles, E.N.; Castillo-Robles, J.A.; Rodríguez-García, J.A. Synthesis of $SrTiO_3$ by the Calcination of $SrCO_3$ and TiO_2 Mixtures Intensively Ground by Means of High Energy Milling. *Arch. Met. Mater.* **2020**, *65*, 621–626. [CrossRef]
15. Roy, P.K.; Bera, J. Formation of $SrTiO_3$ from Sr-Oxalate and TiO_2. *Mater. Res. Bull.* **2005**, *40*, 599–604. [CrossRef]
16. Abedi, M.; Szamosvölgyi, Á.; Sápi, A.; Kukovecz, Á.; Kónya, Z.; Gyulavári, T.; Pap, Z. Influence of Rapid Heat Treatment on the Photocatalytic Activity and Stability of Strontium Titanates against a Broad Range of Pollutants. *Catalysts* **2023**, *13*, 219. [CrossRef]

17. Abreu, Y.G.; Soares, J.C.; Moreira, R.L.; Dias, A. Monitoring the Structural and Vibrational Properties in RE-Doped $SrTiO_3$ Ceramic Powders. *J. Phys. Chem. C* **2016**, *120*, 16960–16968. [CrossRef]
18. Nilsen, W.G.; Skinner, J.G. Raman Spectrum of Strontium Titanate. *J. Chem. Phys.* **1968**, *48*, 2240–2248. [CrossRef]
19. Scott, J.F. Soft-mode spectroscopy: Experimental studies of structural phase transitions. *Rev. Mod. Phys.* **1974**, *46*, 83–128. [CrossRef]
20. Yao, D.; Zhou, X.; Ge, S. Raman scattering and room temperature ferromagnetism in Co-doped $SrTiO_3$ particles. *Appl. Surf. Sci.* **2011**, *257*, 9233–9236. [CrossRef]
21. Vento-Lujano, E.; González, L.A. Defect-induced modification of band structure by the insertion of Ce^{3+} and Ce^{4+} in $SrTiO_3$: A high-performance sunlight-driven photocatalyst. *Appl. Surf. Sci.* **2021**, *569*, 151044. [CrossRef]
22. Šetinc, T.; Spreitzer, M.; Vengust, D.; Jerman, I.; Suvorov, D. Inherent defects in sol-precipitation/hydrothermally derived $SrTiO_3$ nanopowders. *Ceram. Int.* **2013**, *39*, 6727–6734. [CrossRef]
23. Perry, C.H.; Fertel, J.H.; McNelly, T.F. Temperature Dependence of the Raman Spectrum of $SrTiO_3$ and $KTaO_3$. *J. Chem. Phys.* **1967**, *47*, 1619–1625. [CrossRef]
24. Petzelt, J.; Ostapchuk, T. Infrared and Raman Spectroscopy of Some Ferroelectric Perovskite Films and Ceramics. *J. Optoelectron. Adv. Mater.* **2003**, *5*, 725–733.
25. Orru, R.; Licheri, R.; Locci, A.M.; Cincotti, A.; Cao, G. Consolidation/synthesis of materials by electric current activated/assisted sintering. *Mater. Sci. Eng. R Rep.* **2009**, *63*, 127–287. [CrossRef]
26. Munir, Z.A.; Quach, D.V.; Ohyanagi, M. Electric Current Activation of Sintering: A Review of the Pulsed Electric Current Sintering Process. *J. Am. Ceram. Soc.* **2010**, *94*, 1–19. [CrossRef]
27. Belov, A.A.; Shichalin, O.O.; Papynov, E.K.; Buravlev, I.Y.; Kolodeznikov, E.S.; Kapustina, O.V.; Azon, S.A.; Kondrikov, N.B.; Fedorets, A.N.; Tananaev, I.G. Hybrid Sol–Gel and Spark Plasma Sintering to Produce Perovskite-like $SrTiO_3$ Ceramics for Radioactive Waste Isolation. *J. Compos. Sci.* **2023**, *7*, 421. [CrossRef]
28. Kovalevsky, A.V.; Populoh, S.; Patrício, S.G.; Thiel, P.; Ferro, M.C.; Fagg, D.P.; Frade, J.R.; Weidenkaff, A. Design of $SrTiO_3$-Based Thermoelectrics by Tungsten Substitution. *J. Phys. Chem. C* **2015**, *119*, 4466–4478. [CrossRef]
29. Tokita, M. Progress of Spark Plasma Sintering (SPS) Method, Systems, Ceramics Applications and Industrialization. *Ceramics* **2021**, *4*, 160–198. [CrossRef]
30. Bisquert, J.; Vikhrenko, V.S. Interpretation of the Time Constants Measured by Kinetic Techniques in Nanostructured Semiconductor Electrodes and Dye-Sensitized Solar Cells. *J. Phys. Chem. B* **2004**, *108*, 2313–2322. [CrossRef]
31. Prishya, A.A.; Chopra, L. Manikanika Comprehensive review on uses of silicon dioxide in solar cell. *Mater. Today Proc.* **2022**, *72*, 1471–1478. [CrossRef]
32. Zahler, M.P.; Jennings, D.; Kindelmann, M.; Guillon, O.; Rheinheimer, W. Reactive FAST/SPS sintering of strontium titanate as a tool for grain boundary engineering. *J. Eur. Ceram. Soc.* **2023**, *43*, 6925–6933. [CrossRef]
33. Xu, D.; Yuan, Y.; Zhu, H.; Cheng, L.; Liu, C.; Su, J.; Zhang, X.; Zhang, H.; Zhang, X.; Li, J. Nanostructure and Optical Property Investigations of $SrTiO_3$ Films Deposited by Magnetron Sputtering. *Materials* **2019**, *12*, 138. [CrossRef] [PubMed]
34. Goldenberg, E.; Bayrak, T.; Ozgit-Akgun, C.; Haider, A.; Leghari, S.; Kumar, M.; Biyikli, N. Effect of O_2/Ar flow ratio and post-deposition annealing on the structural, optical and electrical characteristics of $SrTiO_3$ thin films deposited by RF sputtering at room temperature. *Thin Solid Films* **2015**, *590*, 193–199. [CrossRef]
35. Photoresponse Mapping of Photovoltaic Cells. Available online: https://api.p1.mks.com/medias/sys_master/images/images/h76/h26/8797239902238/Photoresponse-Mapping-of-Photovoltaic-Cells-App-Note-40.pdf#1#1 (accessed on 4 July 2026).
36. Talanov, M.V.; Stash, A.I.; Ivanov, S.A.; Zhukova, E.S.; Gorshunov, B.P.; Nekrasov, B.M.; Melentev, A.V.; Kozlov, V.I.; Cherepanov, V.M.; Gavrilkin, S.Y.; et al. Transition metal-doped $SrTiO_3$: When does a tiny chemical impact have such a great structural response? *J. Mater. Chem. C* **2024**, *12*, 8105–8118. [CrossRef]